Virtual sensors for local, three dimensional, broadband multiple-channel active noise control and the effects on the quiet zones

P.S. Booij, A.P. Berkhoff
TNO Science & Industry,
Stieltjesweg 1, 2628CK, Delft, The Netherlands
e-mail: **Paul.Booij@tno.nl**

Abstract

In this paper, two state of the art virtual sensor algorithms, i.e. the Remote Microphone Technique (RMT) and the Kalman filter based Virtual Sensing algorithm (KVS) are compared, in both state space (SS) and finite impulse response (FIR) implementations. The comparison focuses on the accuracy of the estimated sound pressure signals at the virtual locations and is based on actual measurements in a practical situation.
The FIR implementation of the RMT algorithm was found to produce the most reliable results. It is implemented in a local, three dimensional, real-time, multiple-channel, broadband active noise control system. With this implementation, the benefits and limitations of the RMT-ANC system on the shape and size of the quiet zones are investigated.

1 Introduction

Local active noise control (ANC) systems aim at creating quiet zones in a primary noise field by introducing a secondary noise field that (partly) cancels the primary noise field at certain locations. This is generally done by minimizing the sound pressure that is measured by one or more *error sensors*. As a result, the *quiet zones*, i.e. the volumes where the noise reduction exceeds 10 dB, are centered on the error sensors. The quiet zones tend to be small, especially when the undesired noise contains higher frequencies. Therefore, the error sensors should be placed in close proximity to the user's ears, to maximize the perceived noise attenuation. This is not always possible or desirable.

To overcome this problem, various virtual sensor techniques have been proposed [2, 3, 4, 5], of which a comprehensive overview is given in [6]. With these techniques, the sound pressure signals at specific locations, referred to as *virtual locations*, e.g. near the user's ears, are estimated using the measurements of sensors that are placed in more convenient locations, referred to as *physical sensors*. The estimated signals are then minimized by the ANC system, resulting in quiet zones centered on the virtual locations.

This paper focuses on two algorithms: the Remote Microphone Technique (RMT), by Roure and Albarrazin [3] and the Kalman filter based Virtual Sensing algorithm (KVS) by Petersen [5, 7]. The algorithms are compared experimentally in an open loop situation. The RMT was found to produce the most reliable results and it is implemented in a real-time ANC system to assess its practical usability and performance in terms of reduction at the virtual locations and shapes and sizes of the quiet zones.
Elliott et al. [1] have calculated that the quiet zone in a fully diffuse, pure tone sound field is spherical, with a diameter of approximately one tenth of the wavelength of the tone. This result is often used as a rule of thumb in various other active noise control setups, such as broadband multiple-channel active noise control in enclosures. We will investigate if this rule of thumb can be applied to RMT ANC as well.

The remainder of this paper is organized as follows. Section 2 describes the experimental setup that has been used throughout the paper. Section 3 provides some background and terminology on feedforward ANC and introduces the basics of the RMT and KVS algorithms. Section 4 compares the RMT and KVS algorithms in open loop. Section 5 assesses the performance of the active noise control system, using RMT virtual sensors and compares it to the performance of the active noise control system without the use of virtual sensors.

2 Experimental Setup

We consider the 'Silent Chair' in Figure 1, which features three speakers and thirty microphones. The speaker in front of the chair is the primary noise source and the two speakers adjacent to the chair are the secondary noise sources. The goal is to minimize the primary noise at the location of the ears of the user. These two ear locations will be referred to as the virtual locations, accentuated by the two green circles in Figure 1. The red circles in Figure 1 show the locations of four physical microphones that are symmetrically attached to the chair. These locations will be referred to as the physical locations. In the head area of the chair, around the virtual locations, a three-dimensional grid is placed, holding 26 microphones. Two of these microphones measure the two virtual locations, the other 24 are regularly spaced in all three dimensions and enable measurements of the three dimensional quiet zone. The grid is schematically depicted in Figure 2. It is made of a thin, wired fence and is expected to be of minimal acoustical significance for the relatively low frequencies of the primary sound that is used in the experiments. The chair is made of cane, also chosen because of its acoustical transparency for low frequencies.

Figure 1: 'Silent Chair' experimental setup. The red circles show the physical locations, the green circles the virtual locations. The primary source is placed in front of the chair, the two secondary sources on the sides.

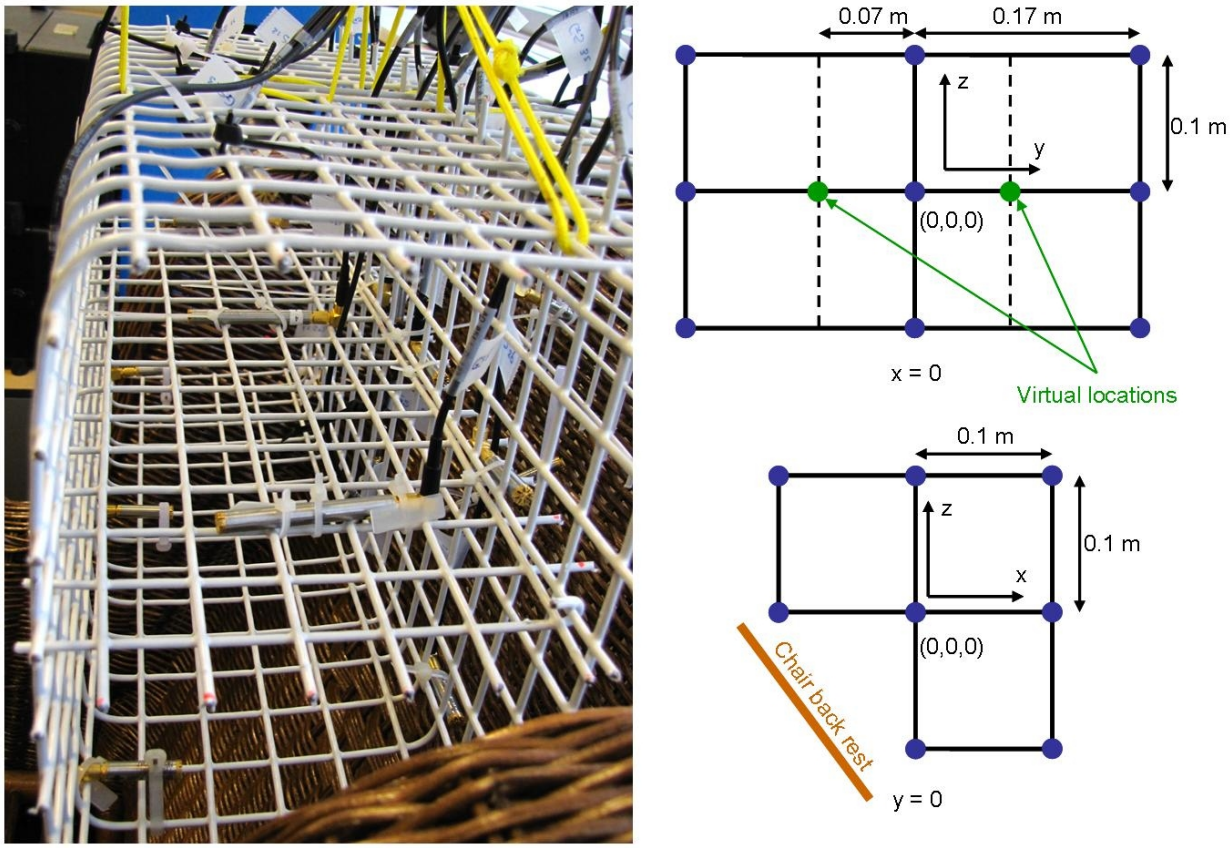

Figure 2: 'Three-dimensional grid for quiet zone measurements'.

2.1 Open loop operation

In Section 4, two virtual sensing algorithms are compared in open loop operation. This means that the active noise control system is not active, but that mutually uncorrelated primary and secondary noise signals are used instead. For these experiments, a setup is used that differs slightly from the setup shown in Figure 1, as only one secondary source is used, which is placed underneath the chair. The grid sensors can also be ignored, as there are no quiet zones in open loop operation, so what remains are six microphones, located at the physical and virtual locations, depicted by the red and green circles respectively. The coordinates of the sources and microphones are give in Table 1.

2.2 Closed loop operation

In Section 5, experiments are done with a closed loop active noise control system, using the setup in Figure 1 and the grid in Figure 2. The coordinates of the sources and microphones are give in Table 1. The microphones used in the control system are Brüel&Kjær, type BK4958 and the grid microphones are a combination of Brüel&Kjær, types BK4958 and similar types BK4957 and BK4935. These are high quality, low-noise microphones.

The two secondary signals are generated by a normalized Filtered-X Least Mean Squares (nFXLMS) algorithm [8], with one reference input, two error inputs and two outputs. The nFXLMS algorithm and the RMT algorithm have been implemented in a real time Linux Xenomai kernel, operating at 2 kHz. All necessary acoustical transfer functions are estimated in a Least Mean Squares (LMS) fashion, in FIR representation.

		Open loop	Closed Loop
Primary source		$(+2.00, \pm 0.00, -0.90)$	$(+2.00, \pm 0.00, -0.90)$
Secondary source	(1)	$(\pm 0.00, \pm 0.00, -1.00)$	$(\pm 0.00, -1.00, \pm 0.00)$
	(2)		$(\pm 0.00, +1.00, \pm 0.00)$
Physical location	(1)	$(\pm 0.00, -0.28, \pm 0.00)$	$(\pm 0.00, -0.28, \pm 0.00)$
	(2)	$(\pm 0.00, +0.28, \pm 0.00)$	$(\pm 0.00, +0.28, \pm 0.00)$
	(3)	$(+0.55, -0.28, -0.42)$	$(+0.55, -0.28, -0.42)$
	(4)	$(+0.55, +0.28, -0.42)$	$(+0.55, +0.28, -0.42)$
Virtual location	(1)	$(\pm 0.00, -0.07, \pm 0.00)$	$(\pm 0.00, -0.07, \pm 0.00)$
	(2)	$(\pm 0.00, +0.07, \pm 0.00)$	$(\pm 0.00, +0.07, \pm 0.00)$

Table 1: Source/sensor *xyz*-coordinates in meters. Orientation and positioning as in Figures 1 and 2.

3 Algorithms

3.1 Feedforward Active Noise Control (ANC)

Consider the ANC scheme in Figure 3. In such a system, unknown disturbance signals $\mathbf{i}(n)$, originating from L_p primary sources, traverse unknown primary paths $\mathbf{G}_p$ and arrive as primary disturbance signals $\mathbf{d}_p(n)$ at the error sensors. Signals $\mathbf{i}(n)$ also traverse unknown reference paths $\mathbf{G}_x$ to M_x reference sensors, resulting in reference signals $\mathbf{x}(n)$. By filtering the acquired reference signals $\mathbf{x}(n)$ with adaptive filters $\mathbf{W}$, L_s secondary signals $\mathbf{u}(n)$ are produced that traverse secondary paths $\mathbf{G}_s$ and arrive at the error sensors as secondary disturbance signals $\mathbf{y}(n)$. The M_e error sensors record the sum of the primary and secondary disturbance signals

$$\mathbf{e}(n) = \mathbf{d}(n) + \mathbf{y}(n). \tag{1}$$

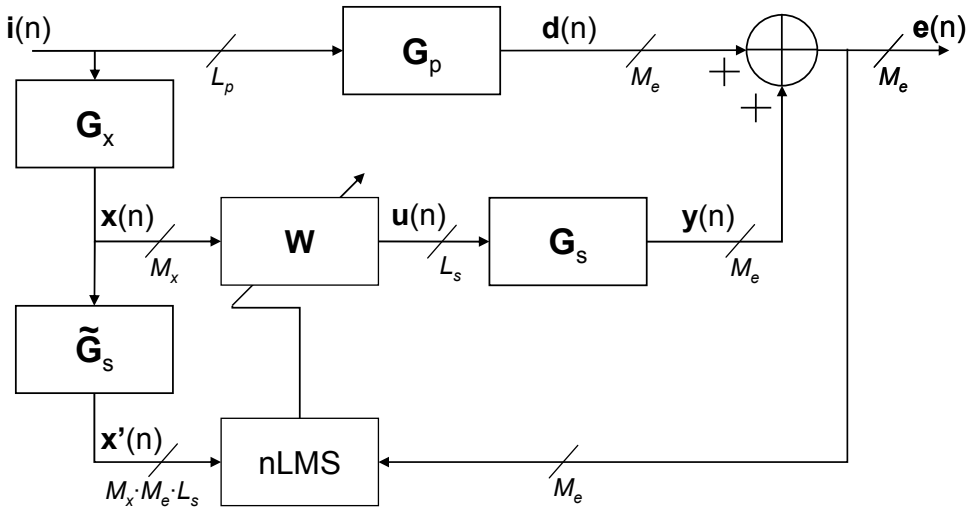

Figure 3: Feedforward nFXLMS Active Noise Control (ANC).

The filters $\mathbf{W}$ are adapted by the nFXLMS algorithm, consisting of the estimated secondary paths $\tilde{\mathbf{G}}_s$ and the nLMS block. Details of the nFXLMS algorithm are out of the scope of this paper, but are widely available in literature, for example in [8].

Note that the ANC scheme of Figure 3 assumes that there is no feedback from the secondary signals $\mathbf{u}(n)$ to the reference signals $\mathbf{x}(n)$. This assumption is valid for the closed loop system described in Section 2, where the primary noise signal $i(n)$ is computer generated and used as reference signal $x(n)$, meaning that $G_x = 1$.

3.2 Virtual sensing

If the ANC scheme in Figure 3 is successful, the energy of the error signals $\mathbf{e}(n)$ will be minimized, resulting in quiet zones around the error microphones. With virtual sensing technology, the virtual error signals $\mathbf{e}_v(n)$ can be minimized instead, which moves the quiet zones to the virtual locations.

The virtual error signals are estimated using measurements at physical locations $\mathbf{e}_p(n)$, the known secondary signals $\mathbf{u}(n)$ and knowledge of the system. This is depicted in Figure 4. Note that the error sensors are discerned into physical and virtual error sensors at the physical and virtual locations, respectively. The secondary paths $\mathbf{G}_s$ have been split into physical secondary paths $\mathbf{G}_{pu}$ and virtual secondary paths $\mathbf{G}_{vu}$ and the primary paths $\mathbf{G}_i$ have been split similarly into $\mathbf{G}_{pi}$ and $\mathbf{G}_{si}$. Equation 1 is extended to

$$\begin{aligned} \mathbf{e}_p(n) &= \mathbf{d}_p(n) + \mathbf{y}_p(n) \\ \mathbf{e}_v(n) &= \mathbf{d}_v(n) + \mathbf{y}_v(n). \end{aligned} \tag{2}$$

Because the estimates of the virtual error signals $\tilde{\mathbf{e}}_v(n)$ are inserted into the ANC system, there is no need to maintain sensors at the virtual locations.

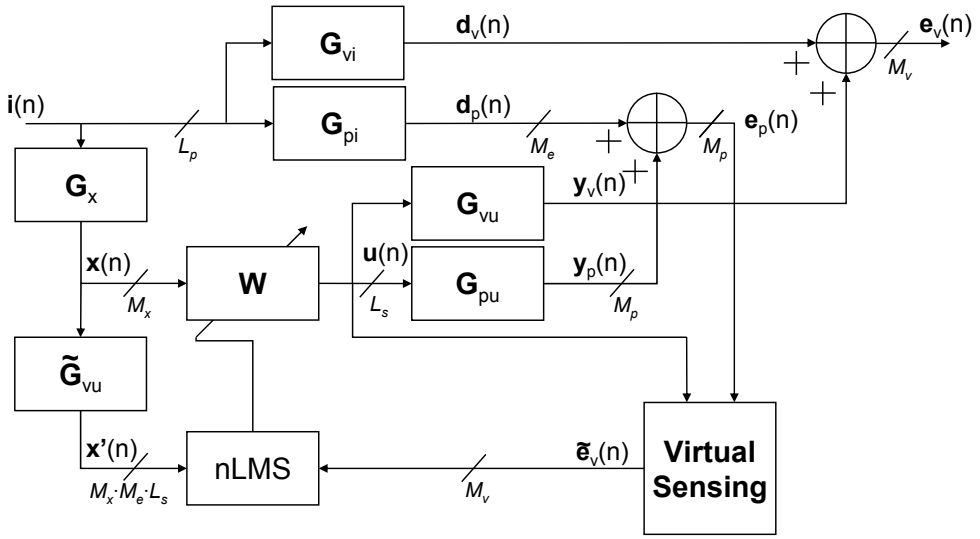

Figure 4: Feedforward nFXLMS Active Noise Control (ANC) with virtual sensing.

3.2.1 Remote Microphone Technique (RMT)

One way to implement the Virtual Sensing block from Figure 4 is with the Remote Microphone Technique, shown in Figure 5. The RMT estimates the virtual error signal in two parts, according to

$$\tilde{\mathbf{e}}_v(n) = \tilde{\mathbf{d}}_v(n) + \tilde{\mathbf{y}}_v(n), \tag{3}$$

which follows from Figure 4. Before usage, the RMT has to be initialized, a procedure that can be described in four steps:

1. Sensors are placed at the virtual locations. Because these are real (physical) sensors at the virtual locations, we will refer to them as *physual sensors*. An input-output data set $\left\{ \mathbf{u}(n), \begin{bmatrix} \mathbf{e}_p(n) \\ \mathbf{e}_v(n) \end{bmatrix} \right\}_{n=1\ldots\eta}$ with η samples is measured.

2. Using the secondary signals $\mathbf{u}(n)$ and the physical and physual measurements $\mathbf{e}_p$ and $\mathbf{e}_v$, the secondary paths $\mathbf{G}_{pu}$ and $\mathbf{G}_{vu}$ are estimated, resulting in the estimated secondary paths $\tilde{\mathbf{G}}_{pu}$ and $\tilde{\mathbf{G}}_{vu}$.

3. The physical and virtual disturbance signals are estimated according to

$$\begin{aligned}\tilde{\mathbf{d}}_p(n) &= \mathbf{e}_p(n) - \tilde{\mathbf{y}}_p(n)\\ \tilde{\mathbf{d}}_v(n) &= \mathbf{e}_v(n) - \tilde{\mathbf{y}}_v(n),\end{aligned} \tag{4}$$

   with $\tilde{\mathbf{y}}_p(n)$ and $\tilde{\mathbf{y}}_v(n)$ calculated with $\mathbf{u}(n)$ and $\tilde{\mathbf{G}}_{pu}$ and $\tilde{\mathbf{G}}_{vu}$ from step 2. Then, transfer function $\tilde{\mathbf{H}}$ that links $\tilde{\mathbf{d}}_p$ to $\tilde{\mathbf{d}}_v$ is estimated.

4. The physual sensors at the virtual locations are removed.

After these initialization steps, transfer functions $\tilde{\mathbf{G}}_{pu}$, $\tilde{\mathbf{G}}_{vu}$ and $\tilde{\mathbf{H}}$ are estimated, which enables estimation of the virtual error signals $\tilde{\mathbf{e}}_v$ according to Figure 5.

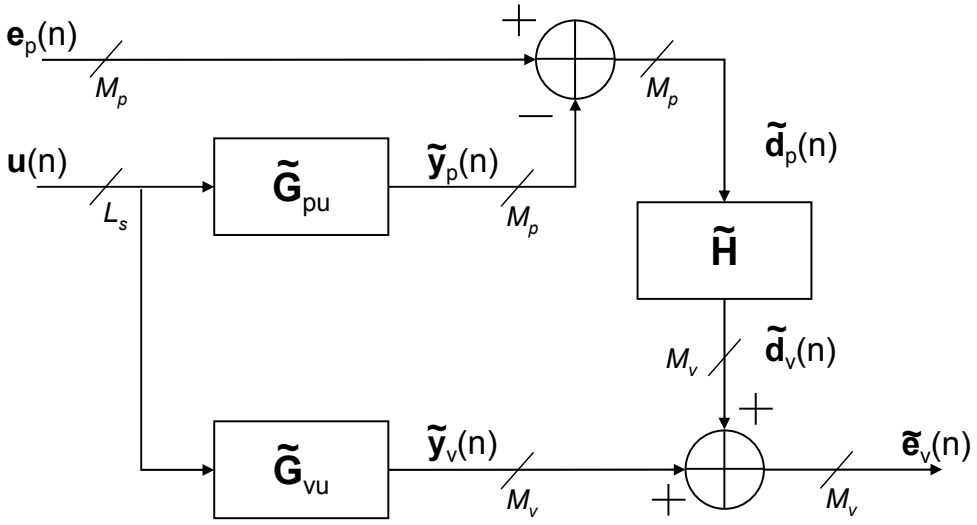

Figure 5: Remote Microphone Technique (RMT).

Note that for proper functioning of the RMT, the correlation between $\mathbf{d}_p(n)$ and $\mathbf{d}_v(n)$ should be causal. Otherwise, transfer function $\tilde{\mathbf{H}}$ can not fully model the relationship between them. To ensure causality, at least one physical sensor should be placed between the primary sources and the virtual locations. The two physical sensors attached near the front of the chair in Figure 1 are placed there for just that reason.

The RMT is based solely on transfer function estimation. The accuracy of the estimated transfer functions determines the performance of the RMT virtual sensors. The transfer functions can be estimated in various ways, using various representations. This paper focuses on the State Space (SS) and Finite Impulse Response (FIR) representations only. The estimation procedures are briefly described in Section 4.

3.2.2 Kalman filter based Virtual Sensing (KVS)

In the KVS algorithm, the system is modeled by an N$^{\text{th}}$ order State Space (SS) model, according to [7]

$$\begin{aligned}\mathbf{z}(n+1) &= \mathbf{A}\mathbf{z}(n) + \mathbf{B}_u\mathbf{u}(n) + \mathbf{w}(n)\\ \mathbf{e}_p(n) &= \mathbf{C}_p\mathbf{z}(n) + \mathbf{D}_{pu}\mathbf{u}(n) + \mathbf{v}_p(n)\\ \mathbf{e}_v(n) &= \mathbf{C}_v\mathbf{z}(n) + \mathbf{D}_{vu}\mathbf{u}(n) + \mathbf{v}_v(n),\end{aligned} \tag{5}$$

with $\mathbf{z}(n)$ the state vector, $\mathbf{w}(n)$ the process noise, according to

$$\mathbf{w}(n) = \mathbf{B}_i\mathbf{i}(n), \tag{6}$$

and $\mathbf{v}_p(n)$ and $\mathbf{v}_v(n)$ according to

$$\begin{aligned} \mathbf{v}_p &= \mathbf{D}_{pi}\mathbf{i}(n) + \boldsymbol{\upsilon}_p(n) \\ \mathbf{v}_v &= \mathbf{D}_{vi}\mathbf{i}(n) + \boldsymbol{\upsilon}_v(n), \end{aligned} \tag{7}$$

with $\boldsymbol{\upsilon}_p(n)$ and $\boldsymbol{\upsilon}_v(n)$ the measurement noise signals of the physical and virtual sensors respectively. Signals $\mathbf{i}(n)$, $\boldsymbol{\upsilon}_p(n)$ and $\boldsymbol{\upsilon}_v(n)$ are assumed to be realizations of zero mean, unit variance, stationary processes that are mutually uncorrelated. Matrices $\mathbf{A}_s, \mathbf{B}_u, \mathbf{B}_i, \mathbf{C}_p, \mathbf{C}_v, \mathbf{D}_{pu}, \mathbf{D}_{vu}, \mathbf{D}_{pi}$ and $\mathbf{D}_{vi}$ are State Space matrices.

The KVS algorithm uses a Kalman filter that provides an estimate $\tilde{\mathbf{z}}(n|n-1)$ of the internal states, using physical measurements $\mathbf{e}_p(n)$ up to time $n-1$ according to

$$\begin{aligned} \tilde{\mathbf{z}}(n+1|n) &= \mathbf{A}\tilde{\mathbf{z}}(n|n-1) + \mathbf{B}_u\mathbf{u}(n) + \mathbf{K}_{pi}\boldsymbol{\epsilon}_p(n) \\ \tilde{\mathbf{e}}_p(n|n-1) &= \mathbf{C}_p\tilde{\mathbf{z}}(n|n-1) + \mathbf{D}_{pu}\mathbf{u}(n), \end{aligned} \tag{8}$$

with $\boldsymbol{\epsilon}_p(n)$ the innovation signals, given by

$$\boldsymbol{\epsilon}_p(n) = \mathbf{e}_p - \tilde{\mathbf{e}}_p(n|n-1), \tag{9}$$

and $\mathbf{K}_{pi}$ the Kalman gain matrix.

Innovation signals $\boldsymbol{\epsilon}_p(n)$ from Equation 9 provide information on the physical, primary disturbance signals $\mathbf{d}_p(n)$ and the physical measurement noise signals $\boldsymbol{\upsilon}_p(n)$. This information is linked to the estimated virtual error signals $\tilde{\mathbf{e}}_v(n)$ by the innovation gain matrix $\mathbf{M}_{vi}$, as seen in Figure 6.

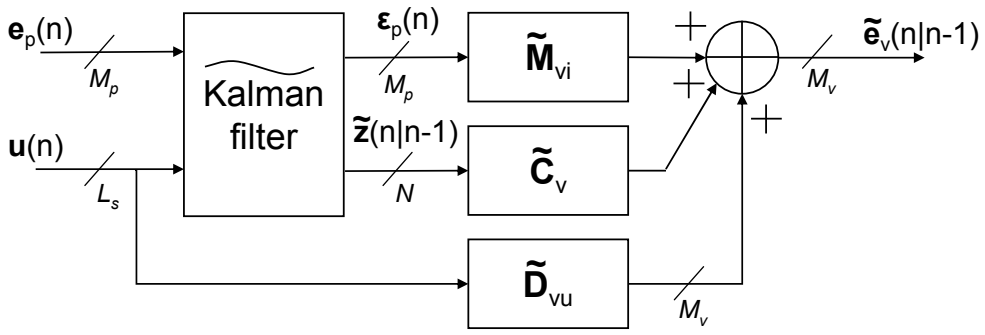

Figure 6: Kalman based Virtual Sensing algorithm (KVS).

Before usage, the KVS algorithm has to be initialized, a procedure that can be described in four steps [6, 7]:

1. Physual sensors are placed at the virtual locations and an input-output data set $\left\{ \mathbf{u}(n), \begin{bmatrix} \mathbf{e}_p(n) \\ \mathbf{e}_v(n) \end{bmatrix} \right\}_{n=1\ldots\eta}$ is measured.

2. Using subspace identification techniques [9] on the input-output data set, the innovations model of the physical and virtual error signals is estimated, yielding

$$\begin{aligned} \tilde{\mathbf{z}}(n+1|n) &= \tilde{\mathbf{A}}\tilde{\mathbf{z}}(n|n-1) + \tilde{\mathbf{B}}_u\mathbf{u}(n) + \tilde{\mathbf{K}}_i \begin{bmatrix} \boldsymbol{\epsilon}_p(n) \\ \boldsymbol{\epsilon}_v(n) \end{bmatrix} \\ \mathbf{e}_p(n) &= \tilde{\mathbf{C}}_p\tilde{\mathbf{z}}(n|n-1) + \tilde{\mathbf{D}}_{pu}\mathbf{u}(n) + \boldsymbol{\epsilon}_p(n) \\ \mathbf{e}_v(n) &= \tilde{\mathbf{C}}_v\tilde{\mathbf{z}}(n|n-1) + \tilde{\mathbf{D}}_{vu}\mathbf{u}(n) + \boldsymbol{\epsilon}_v(n), \end{aligned} \tag{10}$$

   and the covariance matrix of the white innovation signals is estimated according to

$$\tilde{\mathbf{R}} = \begin{bmatrix} \tilde{\mathbf{R}}_p & \tilde{\mathbf{R}}_{pv} \\ \tilde{\mathbf{R}}_{pv}^{\mathsf{T}} & \tilde{\mathbf{R}}_v \end{bmatrix} = \mathbb{E}\left\{ \begin{bmatrix} \boldsymbol{\epsilon}_p \\ \boldsymbol{\epsilon}_v \end{bmatrix} \begin{bmatrix} \boldsymbol{\epsilon}_p & \boldsymbol{\epsilon}_v \end{bmatrix} \right\}, \tag{11}$$

   with $\mathbb{E}$ the expectation operator and $(\cdot)^{\mathsf{T}}$ denoting the transpose.

3. The estimated Kalman gain matrix $\tilde{\mathbf{K}}_{pi}$ is acquired by

$$\tilde{\mathbf{K}}_{pi} = \left(\tilde{\mathbf{A}}\mathbf{X}_i\tilde{\mathbf{C}}_p^{\mathsf{T}} + \tilde{\mathbf{K}}_i\begin{bmatrix}\tilde{\mathbf{R}}_p \\ \tilde{\mathbf{R}}_{pv}^{\mathsf{T}}\end{bmatrix}\right)\left(\tilde{\mathbf{C}}_p\mathbf{X}_i\tilde{\mathbf{C}}_p^{\mathsf{T}} + \tilde{\mathbf{R}}_p\right)^{-1} \tag{12}$$

and the innovation gain matrix is estimated as

$$\tilde{\mathbf{M}}_{vi} = \left(\tilde{\mathbf{C}}_v\mathbf{X}_i\tilde{\mathbf{C}}_p^{\mathsf{T}} + \tilde{\mathbf{R}}_{pv}^{\mathsf{T}}\right)\left(\tilde{\mathbf{C}}_p\mathbf{X}_i\tilde{\mathbf{C}}_p^{\mathsf{T}} + \tilde{\mathbf{R}}_p^{\mathsf{T}}\right)^{-1}, \tag{13}$$

with $\mathrm{X}_i = \mathrm{X}_i^{\mathsf{T}} > 0$ the unique solution to the discrete Ricatti equation given by

$$\mathbf{X}_i = \tilde{\mathbf{A}}\mathbf{X}_i\tilde{\mathbf{A}}^{\mathsf{T}} - \tilde{\mathbf{K}}_{pi}\left(\tilde{\mathbf{C}}_p\mathbf{X}_i\tilde{\mathbf{C}}_p^{\mathsf{T}} + \tilde{\mathbf{R}}_p\right)^{-1}\tilde{\mathbf{K}}_{pi}^{\mathsf{T}} + \tilde{\mathbf{K}}_i\tilde{\mathbf{R}}\tilde{\mathbf{K}}_i^{\mathsf{T}}. \tag{14}$$

4. The physual sensor at the virtual locations are removed.

With the State Space matrices from step 2 and the Kalman and innovation gain matrices from step 3, the KVS can be constructed according to Figure 6.

Petersen [7] has shown that the Kalman based virtual sensor algorithm is equivalent to the remote microphone technique in case of zero measurement noise. In case of non-zero measurement noise, the KVS algorithm theoretically outperforms the RMT.

4 Comparison of the virtual sensor algorithms in open loop

The RMT and KVS algorithms are compared using the open loop configuration of the experimental setup described in Section 2. Three algorithm implementations are tested: RMT in FIR, RMT in SS and KVS in SS (note that a FIR implementation of KVS does not exist). Mutually uncorrelated white noise is played by the primary and secondary sources simultaneously. The data sets are recorded with a sampling frequency of $F_s = 4096$ Hz.

The FIR estimation of the secondary paths $\tilde{\mathbf{G}}_{pu}$ and $\tilde{\mathbf{G}}_{vu}$ and filter $\tilde{\mathbf{H}}$ of the RMT, is done in a least squares sense, using the Matlab routine arx [10]. One data set of 20 seconds duration is used, in which both the primary and secondary noise sources are active. This data set is split equally in two parts. One is used for model estimation, the other for model verification. The filter orders have been chosen experimentally. A filter order of $N_G = 400$ for the secondary paths $\tilde{\mathbf{G}}_{pu}$ and $\tilde{\mathbf{G}}_{vu}$ and $N_H = 200$ for transfer function $\tilde{\mathbf{H}}$ were found to provide reliable results.

The SS estimation is done in Matlab using the SLICOT subspace identification routines [11]. A two-step identification procedure [7] was chosen, where the parametric part of the SS model is estimated using a data set without a primary noise signal (i.e. $i(n) = 0$) and the stochastic part is estimated using a data set without secondary noise signals (i.e. $\mathbf{u}(n) = \mathbf{0}$). Both data sets have a duration of 20 seconds and are again split in an estimation and a verification part. Note that in practice, obtaining a data set with $i(n) = 0$ might not always be possible.

The SS model order was chosen experimentally, but was limited by numerical instability and limited computer resources. A model order of $N = 400$, (using 800 block rows in the Hankel matrices), was found to provide acceptable results for the secondary paths. Higher orders could not be calculated due to memory limitations on a 2.6 GHz, dual core machine with 2 GB of RAM. Note that a SS order of 400 is quite high, yet in this case still below optimal. This is caused by the relatively high sample rate of $F_s = 4096$ Hz. Reducing the sampling rate of the data during preprocessing would be a good option, however, this was found to reduce the numerical stability of the SLICOT routines severely. More specifically, it seems that when the resemblance between some of the signal vectors in the input-output data set increases, the SLICOT routines become increasingly more ill-conditioned. This could explain the found sensitivity for down sampling of the

data set, since the low frequency contents of the signals show large mutual resemblance due to the wavelengths being large, relative to the distances between the sensor positions. It would also explain why it has been impossible to accurately estimate an SS model of $\tilde{\mathbf{H}}$, because of the small distances between some of the physical sensors and the virtual sensors, which causes the input and output data sets to be very similar.

The performance of the virtual sensing algorithms and the accuracy of the estimated transfer functions is evaluated by means of the Variance Accounted For (VAF), which compares the estimated and measured signals from a data set $\{\tilde{\mathbf{e}}_v(n), \mathbf{e}_v(n)\}_{n=1...\eta}$ for each estimated signal $\tilde{e}_{v_j}(n)$ in $\tilde{\mathbf{e}}_v(n)$ and states how well the output is explained by the model. It does so by assigning a score between $0 - 100\%$, according to

$$\mathrm{VAF}_j = \max\left(1 - \frac{\mathrm{var}\left\{e_{v_j}(n) - \tilde{e}_{v_j}(n)\right\}}{\mathrm{var}\left\{e_v(n)\right\}}, 0\right) \cdot 100\%, \tag{15}$$

with the variance according to

$$\mathrm{var}\left\{e_{v_j}(n)\right\} = \mathbb{E}\left\{e_{v_j}^2(n)\right\} - \mathbb{E}\left\{e_{v_j}(n)\right\}^2, \tag{16}$$

and $j = 1...J$. An average VAF value can be give for the entire data set according to

$$\overline{\mathrm{VAF}} = \frac{1}{J}\sum_{j=1}^{J} \mathrm{VAF}_j. \tag{17}$$

4.1 Results

The results of the RMT and KVS algorithms in FIR and SS implementations are summarized in Table 2. Note that the results of the SS RMT algorithm are dramatic, because SS estimation of transfer function $\tilde{\mathbf{H}}$ was numerically infeasible, as previously explained. Also note that the $\overline{\mathrm{VAF}}$ value of the secondary paths in the FIR RMT case is only 65.09%. This is to be expected, since a data set with both primary and secondary noise signals was used for validation and the estimated models $\tilde{\mathbf{G}}_{pu}$ and $\tilde{\mathbf{G}}_{vu}$ only relate to the secondary noise signals. For sake of comparison, using a data set with $s(n) = 0$ for model validation yields a $\overline{\mathrm{VAF}}$ value of 98.54%.

Figure 7 shows the spectral estimation error for each estimated signal $\tilde{e}_{v_j}(n)$ in $\tilde{\mathbf{e}}_v(n)$, according to

$$\Psi_{v_j} = 10\log_{10}\left(\frac{\mathcal{P}_{\epsilon_{v_j}}}{\mathcal{P}_{e_{v_j}}}\right), \tag{18}$$

with $\mathcal{P}_{e_{v_j}}$ the Power Spectral Density (PSD) of signal e_{v_j} and

$$\epsilon_{v_j} = \tilde{e}_{v_j} - e_{v_j}. \tag{19}$$

The PSDs in Figure 7 are calculated using Welch's method [12] with a window size of 75 samples, a window overlap of 50 samples and an FFT length of 1024. The blue and green spectra represent the left and right virtual locations respectively. From the figure, it is clear that the FIR RMT algorithm outperforms the SS KVS algorithm. The FIR RMT algorithm is accurate up to approximately 43% of the sampling rate.

Algorithm	Implementation	Secondary Paths $\overline{\mathrm{VAF}}$	RMT filter $\tilde{\mathbf{H}}$ $\overline{\mathrm{VAF}}$	**Virtual Sensing** $\overline{\mathrm{VAF}}$
RMT	FIR	65.09%	98.03%	$\mathbf{99.36}\%$
RMT	SS	95.19%	00.00%	$\mathbf{00.00}\%$
KVS	SS	95.19%	-	$\mathbf{93.78}\%$

Table 2: Comparison of the RMT and KVS algorithms in terms of $\overline{\mathrm{VAF}}$ values.

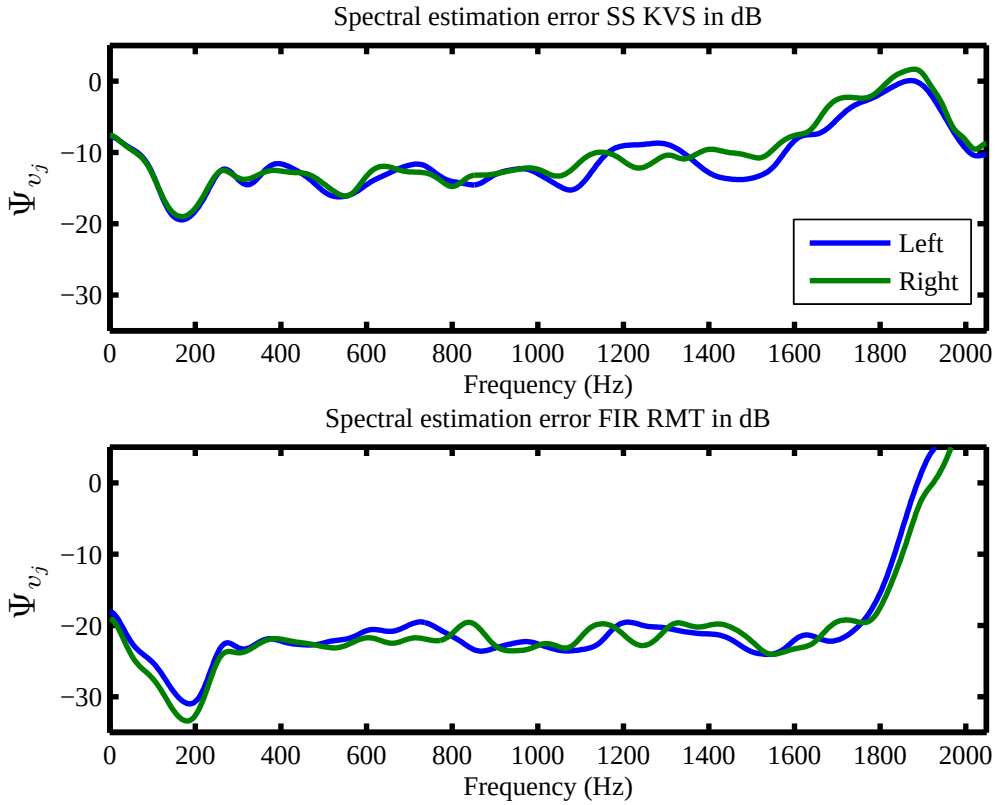

Figure 7: Comparison of the spectral estimation error between SS KVS and FIR RMT.

4.2 Open loop algorithm conclusions

The performance of the RMT and KVS algorithms are determined most significantly by the accuracy of the estimated models. Measurement noise will usually, and especially in this case with high quality microphones, play a less significant role. The subspace estimation algorithms currently available are not yet as accurate and robust as the FIR estimation techniques, especially for highly dynamic systems that require a high model order.

In virtual sensing situations where model accuracy is of utmost importance (e.g. the setup in Figure 1), it is recommended to use a FIR based virtual sensing algorithm. Since the KVS algorithm is only available in SS, the FIR RMT algorithm is currently the better option in these situations.

5 Closed Loop Performance with RMT Virtual Sensing

The RMT algorithm is tested in the ANC setup from Figure 1. Three situations are compared:

1. Measurements from the two physical sensors on the sides of the chair at ear level (physical locations 1 and 2 in Table 1) are used as error signals. These signals are minimized by the ANC system. This would be the best attempt to reduce the noise at the virtual locations without placing error sensors at those locations or using virtual sensing techniques.

2. Measurements from the two physual sensors at the virtual locations are used as error signals and are minimized by the ANC system. This will provide the best possible reduction at the virtual locations, but comes with the price that microphones have to be positioned at the virtual locations.

3. RMT virtual sensing is used to estimate the error signals at the virtual locations. This way, there is no need for placing microphones at the virtual locations, but estimation errors of the RMT will result in lower reduction, compared to situation 2.

The initialization procedure from Section 3.2.1 is carried out slightly different, as a two-step identification approach is used instead. In the first step, pink noise is played by each secondary source in turn, in absence of primary noise and the secondary paths $\tilde{\mathbf{G}}_{pu}, \tilde{\mathbf{G}}_{vu}$ between each actuator and the physical and virtual sensors are estimated. This results in an average secondary path VAF value of $\overline{\mathrm{VAF}} = 98.84\%$. In the second step, the secondary sources are turned off and the primary source plays pink noise. The transfer functions $\tilde{\mathbf{H}}$ are estimated. This results in an average VAF value for filters $\tilde{\mathbf{H}}$ of $\overline{\mathrm{VAF}} = 98.99\%$.

Two measurement sets at the virtual locations and at the grid locations are acquired for all three situations. The first set is the reference measurement, where only pink primary noise is present and the secondary sources and ANC system are turned off. The second set is a measurement with all sources on and after the ANC system has adapted for five minutes, to ensure that the ANC algorithm has reached steady state. The reduction $\boldsymbol{\Delta}_v = \begin{bmatrix}\Delta_{v_l} & \Delta_{v_r}\end{bmatrix}^\mathsf{T}$ at the left and right virtual locations respectively, is then spectrally calculated by comparison of the two data sets, according to

$$\mathcal{P}_{\Delta_j} = 10\log_{10}\left(\frac{\mathcal{P}_{e_{v_{j,\mathrm{off}}}}}{\mathcal{P}_{e_{v_{j,\mathrm{on}}}}}\right), \tag{20}$$

with $e_{v_{j,\mathrm{off}}}$ and $e_{v_{j,\mathrm{on}}}$ the measurements at virtual location j with the ANC system turned off and on respectively and $\mathcal{P}$ again the PSD, calculated using Welch's method [12].

5.1 Results

Figure 8 shows the reduction at the virtual locations for each situation spectrally, up to 500 Hz. For situation 1, the reduction of the error signals (at the first 2 physical locations) is shown as well. From the figure, it is clear that situation 1 achieves significant (> 10 dB) reduction at the virtual locations between 30 and 90 Hz only. For higher frequencies, the quiet zones get smaller and do not extend to the virtual locations anymore. In situation 2, proper reduction at the virtual locations is achieved over the entire bandwidth of interest, with exception for the very low frequencies, which are uncontrollable by the speakers and are therefore not present in the primary nor secondary noise. Situation 3 shows comparable behavior to situation 2, although the overall performance is 26.36% lower. This difference is caused by estimation errors of the RMT. More specifically, by inaccuracies in the estimated paths $\tilde{\mathbf{G}}_{pu}, \tilde{\mathbf{G}}_{vu}$ and $\tilde{\mathbf{H}}$, as stated by [3, 6].
Figure 8 also shows the x, y, z profiles of the three-dimensional quiet zones. Note that these figures show the average reduction in dB over the entire 0-500 Hz bandwidth. The blue dots show the locations of the grid sensors, the black dots the locations of the virtual locations. Spline interpolation is used to increase the resolution of these plots.

When observing the quiet zones as function of frequency, it strikes that these zones are not consistently shaped. For some frequency ranges, where the room exhibits significant modal acoustics, the quiet zones are increasingly ellipsoidal and show irregularities. Truly spherical quiet zones are exception, rather than rule in the performed measurements.

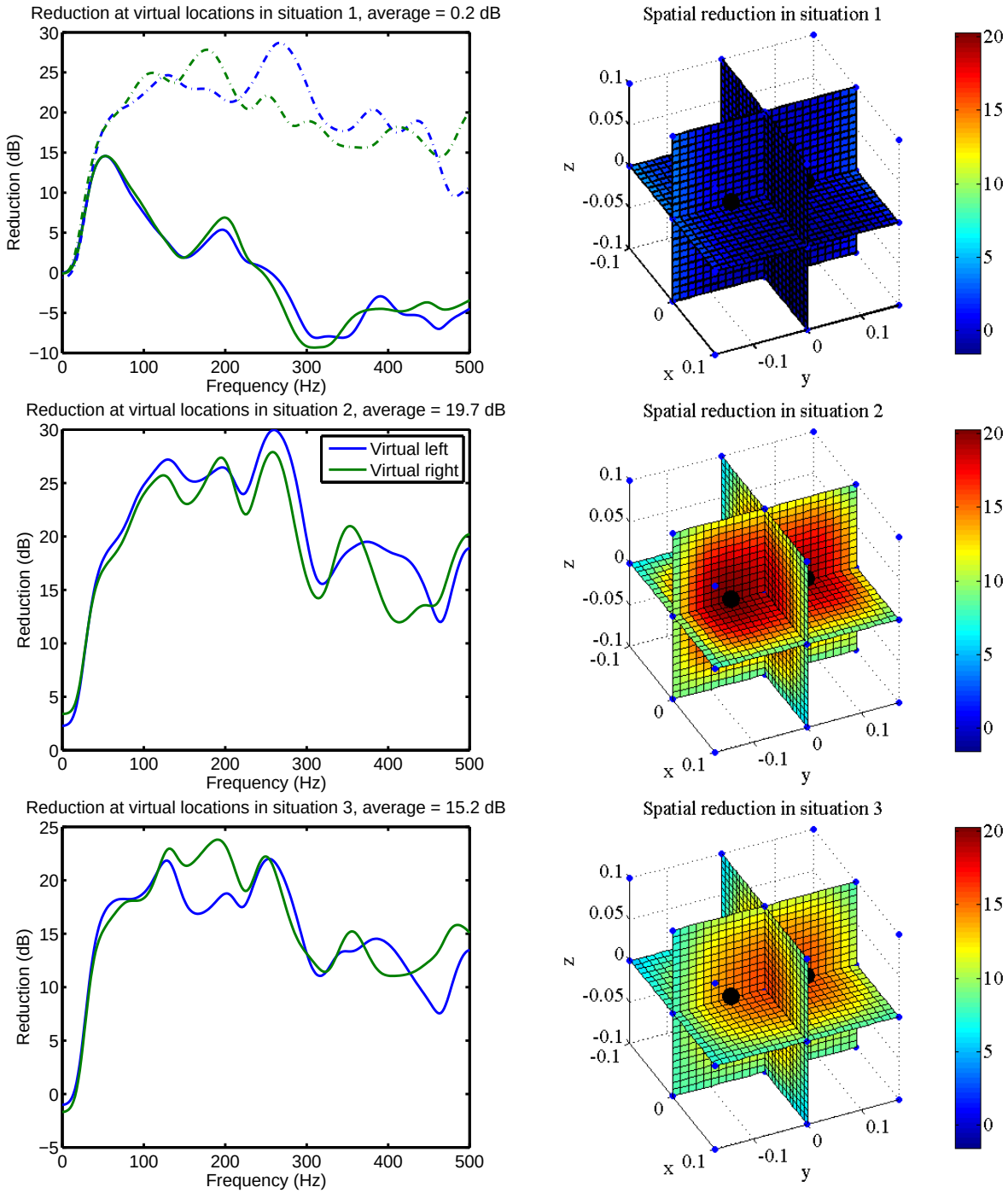

Figure 8: Left: Achieved spectral reduction as measured at the virtual locations, for all three situations. The dotted lines in the top left plot represent the spectral reduction at the two physical locations where the minimization is performed. The average reduction for the two locations in the 0-500 Hz range is given for each situation. Right: Spatial reduction, averaged over the 0-500 Hz range, as measured by the sensor grid and the physual sensors. The blue dots represent the grid sensors, the large black dots represent the physual sensors.

The volumes of the quiet zones also develop quite erratically as a function of frequency. Instead of a continuous decrease of volume for increasing frequencies, it turns out that the system performance (i.e. the reduction of the error signals) plays a much larger role in the quiet zone volumes. This is shown in the left part of Figure 9 for situations 2 and 3. The dotted blue line depicts the predicted total volume where reduction exceeds 10 dB (i.e. the union of the left and right quiet zones), according to the rule of thumb that describes spherical quiet zones with diameters of one tenth of the wavelength, given by

$$V(f) = 2\frac{4}{3}\pi r(f)^3 \quad r(f) \leq \frac{\rho}{2} \tag{21}$$

with $\rho = 0.14$ meters, the distance between the two virtual locations. For radii larger than $\frac{\rho}{2}$, Equation 21 does not hold, as the two quiet zones will intersect. This situation does not occur in our analysis.
The rule of thumb dictates a radius per quiet zone $r(f)$ of

$$r(f) = \frac{c}{20f}, \tag{22}$$

with $c \approx 343$ m/s the speed of sound and f the frequency. The solid blue line in Figure 9 depicts the measured volume for frequencies in the 300-500 Hz range. For lower frequencies, the measured quiet zones exceed the grid, so these frequencies are excluded for the analysis. The solid red line, belonging to the red axis at the right of the plot, shows the average reduction at the two virtual locations. The figure clearly shows that the volume of the total quiet zone for a certain frequency depends more significantly on the system's performance at that frequency, than on the frequency itself. Supporting this statement, we observe that the decrease of system's performance caused by the use of RMT virtual sensing (24.4% in the 300-500 Hz range) translates to a 50.7% decrease of the total quiet zone volume.

The measurements also show that the total quiet zone volume always exceeds the predicted volume, even when using RMT virtual sensing, as long as the system's performance exceeds 10 dB reduction. This is the result of the proximity of the two virtual locations, which introduces a certain degree of synergy, especially in the area between the two virtual locations.

The position of the quiet zones changes with frequency as well. The right side of Figure 9 shows the *center of reduction* $\boldsymbol{\chi} = (\chi_x, \chi_y, \chi_z)$ of the total > 10 dB reduction volume for situations 2 and 3 as function of frequency, according to a discrete approximation of

$$\begin{aligned}
\chi_x &= \frac{\int_x x\Delta(x,y,z)}{\int_x \int_y \int_z \Delta(x,y,z)}, \\
\chi_y &= \frac{\int_y y\Delta(x,y,z)}{\int_x \int_y \int_z \Delta(x,y,z)}, \\
\chi_z &= \frac{\int_z z\Delta(x,y,z)}{\int_x \int_y \int_z \Delta(x,y,z)},
\end{aligned} \tag{23}$$

with $\Delta(x, y, z)$ the reduction at coordinates (x, y, z) in dB. The Cartesian deviation from the origin, halfway between the two virtual locations, is given by

$$|\boldsymbol{\chi}|_2 = \sqrt{\chi_x^2 + \chi_y^2 + \chi_z^2}. \tag{24}$$

The figure shows that the displacement of the total quiet zone can be quite extensive. A displacement in the y-direction means movement of the quiet zone from the center in favorite of one of the virtual locations and is therefore not necessarily problematic. However, displacement in the x, y-directions means a movement of the quiet zone away from the virtual locations. In the measurements from situations 2 and 3, there are frequency ranges where one or both virtual locations are not within the total quiet zone, due to a small quiet zone volume and a large quiet zone displacement for this frequencies. These situations occur more frequently in situation 3, where the volume is generally smaller due to the lower system performance.

5.2 Closed loop algorithm conclusions

It is clear that ANC with RMT virtual sensing performs much better than the traditional approach where error sensors are fitted in feasible locations as close to the virtual locations as possible. The average reduction at the two virtual locations, in the $0 - 500$ Hz frequency range is 0.2 dB in the traditional situation and 15.2 dB when using RMT virtual sensing. This is 4.5 dB less than the optimal reduction which could be achieved when placing error sensors at the virtual locations.

It has been shown that the rule of thumb that was proposed by Elliott et al. [1] for active control of a diffuse, pure tone sound field can not be fully expanded to broadband multiple-channel active noise control in enclosures. Synergy between the separate quiet zones causes the total quiet zone volume to be generally larger than the sum of the volumes as stated by the rule of thumb. In this respect, the rule of thumb provides a conservative approximation of the total quiet zone volume, even when using an accurate RMT virtual sensing implementation. However, modal acoustical behavior in the enclosure makes the shape and location of the quiet zones unpredictable to a point that in some cases, the virtual locations are not within the quiet zone. Moreover, it has been shown that the amount of reduction at the error sensors for a certain frequency plays a much more important role in the total quiet zone volume, than the frequency itself. As a result, the loss of system's performance that is introduced by the RMT virtual sensing, translates to a much smaller quiet zone volume.

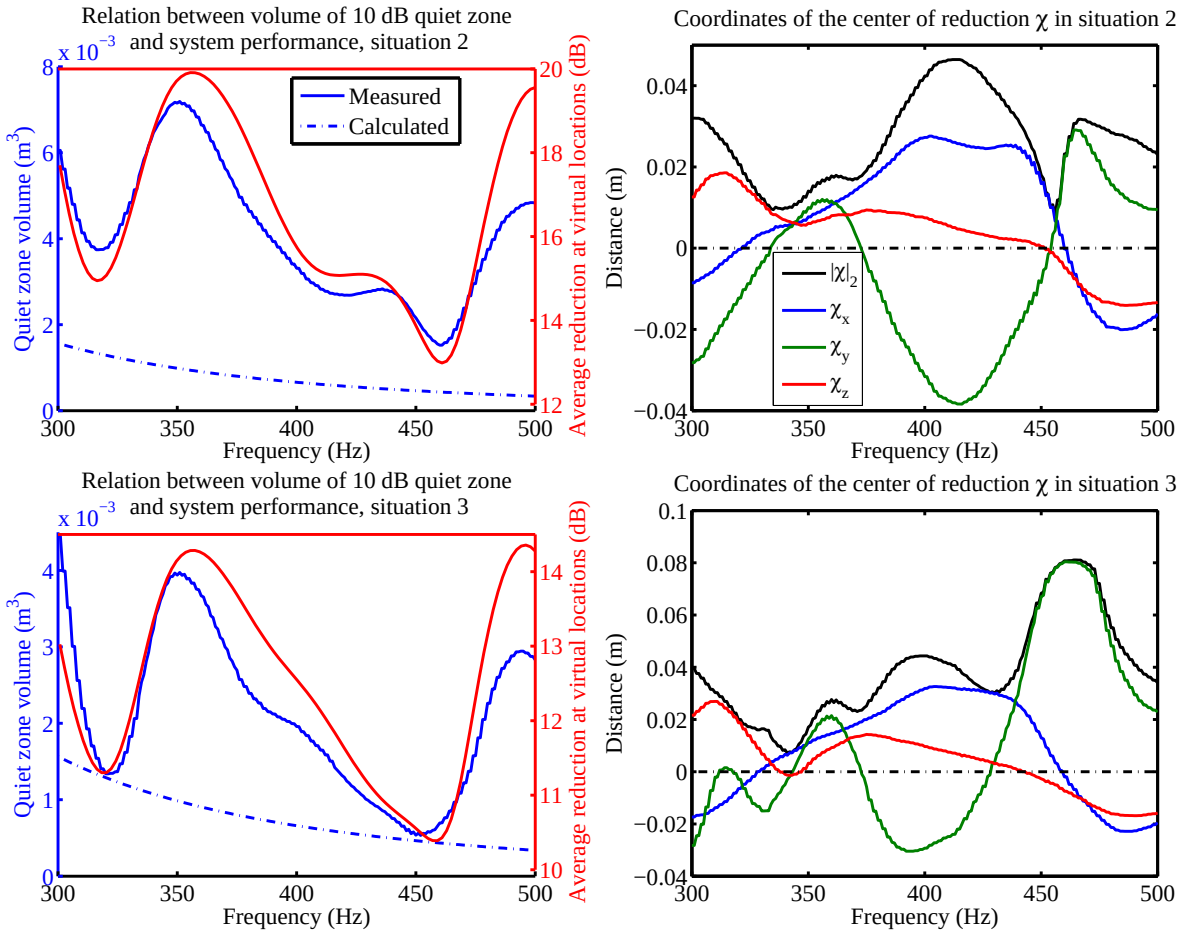

Figure 9: Left: The volume of the total 10 dB quiet zone (i.e. the union of the two quiet zones), measured and calculated according to the rule of thumb [1], in relation to the system's performance, expressed by the average reduction at the virtual locations. Right: The displacement of the center of reduction and its x, y, z coordinates, as function of frequency.

6 Acknowledgements

The authors would like to thank Fraukje Coopmans for her contribution to the closed loop experiments and quiet zone measurements.

References

[1] S. Elliott, P. Joseph, A. Bullmore, P. Nelson, *Active cancellation at a point in a pure tone diffuse sound field*, Journal of Sound and Vibration, Vol. 120, No. 1, 1988, pp. 183-189.

[2] S. Elliott, A. David, *A virtual microphone arrangement for local active sound control*, in *Proceedings of the 1st International Conference on Motion and Vibration Control, Yokohama, Japan, 1992*, Yokohama (1992), pp. 1027-1031.

[3] A. Roure, A. Albarrazin, *The remote microphone technique for active noise control*, in *Proceedings of Active 99, Fort Lauderdale, USA, 1999*, Fort Lauderdale (1999), pp. 1233-1244.

[4] B. Cazzolato, *An adaptive LMS virtual microphone*, in *Proceedings of Active 02, Southhampton, UK, 2002*, Southhampton (2002), pp. 105-116.

[5] C. Petersen, R. Fraanje, B. Cazzolato, A. Zander, C. Hansen, *A Kalman filter approach to virtual sensing for active noise control*, Mechanical Systems and Signal Processing, Vol. 22, No. 2, 2008, pp. 490-508.

[6] D. Moreau, B. Cazzolato, A. Zander, C. Petersen, *A review of virtual sensing algorithms for active noise control*, Algorithms, Vol. 1, No. 2, 2008, pp. 69-99.

[7] C. Petersen, *Optimal spatially fixed and moving virtual sensing algorithms for local active noise control*, Ph.D. Thesis, University of Adelaide, Australia (2007).

[8] S. Kuo, D. Morgan, *Active noise control systems, algorithms and DSP implementations*, Wiley, New York, USA (1996).

[9] L. Haverkamp, *State Space Identification: Theory and Practice*, Ph.D. Thesis, Delft University of Technology, The Netherlands (2001).

[10] The MathWorks, Matlab, System Identification Toolbox, *http://www.mathworks.nl/access/helpdesk/help/toolbox/ident/ref/arx.html*.

[11] The control and systems library SLICOT, *http://www.slicot.org*.

[12] P. Welch, *The use of fast Fourier transform for estimation of power spectra: a method based on time averaging over short, modified periodograms*, IEEE Transactions on Audio Electroacoustics, Vol. AU, No. 15, 1967, pp. 70-73.